

Pressure-tuned structure and superconductivity in 2H-$NbSe_2$

Chen-Yi Li(李晨一), Zong-Lun Li(李宗伦), Hui Tian(田辉), Guang-Rui Gu(顾广瑞), Quan-Jun Li(李全军), and Xue-Ting Zhang(张雪婷)

Citation: Chin. Phys. B, 2026, 35 (**5**): 056401. DOI: 10.1088/1674-1056/ae40db
http://cpb.iphy.ac.cn; http://iopscience.iop.org/cpb

What follows is a list of articles you may be interested in

Tunable thermal conductivity and mechanical properties of metastable silicon by phase engineering

Guoshuai Du(杜国帅), Yubing Du(杜玉冰), Jiaxin Ming(明嘉欣), Zhixi Zhu(朱芷希), Jiaohui Yan(闫皎辉), Jiayin Li(李嘉荫), Tiansong Zhang(张天颂), Lina Yang(杨哩娜), Ke Jin(靳柯), and Yabin Chen(陈亚彬)

Chin. Phys. B, 2025, 34 (**9**): 096401. DOI: 10.1088/1674-1056/adcf8a

Pressure-induced magnetic phase and structural transition in $SmSb_2$

Tao Li(李涛), Shuyang Wang(王舒阳), Xuliang Chen(陈绪亮), Chunhua Chen(陈春华), Yong Fang(房勇), and Zhaorong Yang(杨昭荣)

Chin. Phys. B, 2024, 33 (**6**): 066401. DOI: 10.1088/1674-1056/ad362c

Anomalous bond-length behaviors of solid halogens under pressure

Min Wu(吴旻), Ye-Feng Wu(吴烨峰), and Yi Ma(马毅)

Chin. Phys. B, 2021, 30 (**7**): 076401. DOI: 10.1088/1674-1056/abf4bd

Novel structures and mechanical properties of Zr_2N: *Ab initio* description under high pressures

Minru Wen(文敏儒), Xing Xie(谢兴), Zhixun Xie(谢植勋), Huafeng Dong(董华锋), Xin Zhang(张欣), Fugen Wu(吴福根), and Chong-Yu Wang(王崇愚)

Chin. Phys. B, 2021, 30 (**1**): 016403. DOI: 10.1088/1674-1056/abb220

A high-pressure study of Cr_3C_2 by XRD and DFT

Lun Xiong(熊伦), Qiang Li(李强), Cheng-Fu Yang(杨成福), Qing-Shuang Xie(谢清爽), Jun-Ran Zhang(张俊然)

Chin. Phys. B, 2020, 29 (**8**): 086401. DOI: 10.1088/1674-1056/ab8c3d

---

SPECIAL TOPIC — Structures and properties of materials under high pressure

Pressure-tuned structure and superconductivity in 2H-$NbSe_2$

Chen-Yi Li(李晨一)[1], Zong-Lun Li(李宗伦)[2], Hui Tian(田辉)[3], Guang-Rui Gu(顾广瑞)[4,†], Quan-Jun Li(李全军)[1], and Xue-Ting Zhang(张雪婷)[5,‡]

[1] *State Key Laboratory of High Pressure and Superhard Materials, Jilin University, Changchun* 130012, *China*
[2] *School of Physical Science and Technology, Guangxi University, Nanning* 530004, *China*
[3] *School of Science, Shenyang Ligong University, Shenyang* 110159, *China*
[4] *Department of Physics, College of Science, Yanbian University, Yanji* 133002, *China*
[5] *School of Medical Information Engineering, Shenyang Medical College, Shenyang* 110034, *China*

(Received 1 December 2025; revised manuscript received 20 January 2026; accepted manuscript online 3 February 2026)

The structural and superconducting properties of 2H-$NbSe_2$ were systematically investigated under pressure up to 55.4 GPa using high-pressure electrical transport measurements, synchrotron radiation x-ray diffraction, and theoretical calculations. With increasing pressure, the enhanced interlayer coupling of 2H-$NbSe_2$ induces a structural transition from quasi-two dimensional to three dimensional. Meanwhile, accompanied by Fermi surface reconstruction, 2H-$NbSe_2$ exhibits a characteristic dome-shaped superconducting behavior, which provides valuable insights into the relationship between its superconducting properties and the structural transition.

Keywords: 2H-$NbSe_2$, superconductivity, high pressure, phase transition

PACS: 64.70.Nd, 63.22.Np, 74.25.–q, 74.62.Fj

DOI: 10.1088/1674-1056/ae40db **CSTR:** 32038.14.CPB.ae40db

1. Introduction

The discovery of superconductivity has spurred decades of research aimed at tailoring the superconducting properties of materials.[1,2] Among the various tuning strategies, high pressure has emerged as one of the most effective and versatile modulation techniques. It enables uniform and controllable tuning of lattice parameters and electronic structures without introducing extrinsic impurities or chemical disorder.[3,4] Such lattice compression can enhance electron–phonon interactions and modify interlayer coupling, both of which directly affect the superconducting transition temperature (T_c).[5–7] Consequently, high pressure serves not only as a practical tool for tuning superconductivity but also as a unique probe for elucidating the underlying mechanisms that govern superconducting states.

Transition metal dichalcogenides (TMDs), characterized by the general formula MX_2 (where M denotes a transition metal such as Mo, W, or Re, and X represents a chalcogen such as S, Se, or Te), have garnered significant interest owing to their diverse electronic properties and promising applications in nanoelectronics and optoelectronics.[8–11] Previous investigations have demonstrated that the superconducting behavior of TMDs under pressure is intrinsically coupled to their structural evolution. For instance, in the isostructural compounds 1T-$TiSe_2$ and 1T-$TiTe_2$, pressure-induced structural transitions are associated with the suppression of superconductivity in one case and its emergence in the other.[12–15] Furthermore, distinct polymorphs within the same TMD family can exhibit markedly different superconducting responses. A notable example is 1T-TaS_2, where T_c exhibits a dome-shaped dependence on pressure, peaking at approximately 6 K around 20 GPa. Notably, beyond a structural transition at $\sim$ 45 GPa, T_c displays a renewed increasing trend.[16] Conversely, 2H-TaS_2 shows a different trajectory: its initial superconducting state is re-enhanced above 100 GPa following a suppression near 10 GPa, accompanied by the emergence of an unexpected second superconducting phase at 86.1 GPa.[17] These findings underscore the complex interplay between structural transitions and superconductivity in TMDs under high pressure. Despite significant progress, a comprehensive understanding of these phenomena remains incomplete, necessitating further systematic investigations.

2H-$NbSe_2$ is a type-II superconductor with a typical layered TMD structure, and its T_c of 7.2 K represents the highest value among TMDs at ambient pressure.[18–20] Crystallizing in the $P6_3/mmc$ space group, the layers are separated by an interlayer distance of approximately 6.2 Å and are held together by van der Waals (vdW) interactions.[21,22] This structural configuration renders its superconducting properties highly sensitive to interlayer compression. Although early studies debated whether pressure-induced variations in T_c arise predominantly from reduced interlayer spacing or intralayer distortions,[23,24]

†Corresponding author. E-mail: grgu@ybu.edu.cn
‡Corresponding author. E-mail: syyxy_zxt@163.com

© 2026 Chinese Physical Society and IOP Publishing Ltd. All rights, including for text and data mining, AI training, and similar technologies, are reserved.

more recent angle-resolved photoemission spectroscopy and Raman investigations have revealed that anisotropic electron–phonon coupling across Fermi-surface sheets plays a pivotal role in governing superconductivity in 2H-$NbSe_2$.[25,26] However, the detailed relationship between its structure and T_c remains ambiguous, underscoring the necessity for a comprehensive high-pressure study of 2H-$NbSe_2$.

In this work, we systematically investigate the evolution of the superconducting properties and structure of 2H-$NbSe_2$ upon compression through electrical transport measurements, synchrotron x-ray diffraction (XRD) experiments, and first-principles calculations. With increasing pressure, the interlayer coupling is substantially enhanced, leading to the formation of covalent-like interlayer bonds. We demonstrate that the dome-shaped superconducting behavior of 2H-$NbSe_2$ is intrinsically correlated with the structural transition from quasi-two dimensional (2D) to three dimensional (3D). This study provides critical insights into the relationship between structure and superconducting properties of 2H-$NbSe_2$ under pressure and advances the understanding of pressure-induced phenomena in low-dimensional materials.

2. Experiment methods

The 2H-$NbSe_2$ sample was obtained from HQ Graphene. The ambient-pressure XRD pattern was collected using a Rigaku MicroMax-007HF x-ray diffractometer with Cu $K\alpha$ radiation ($\lambda = 1.5406$ Å). The surface morphology and microstructure were characterized by scanning electron microscopy (SEM, FEI Magellan 400) and high-resolution transmission electron microscopy (HRTEM, JEOL JEM-2200FS), respectively.

High-pressure electrical transport measurements were conducted in symmetric diamond anvil cells (DACs) using T301 stainless-steel gaskets without a pressure-transmitting medium. Two experimental runs were performed to cover different pressure ranges: run 1 (1.1–13.1 GPa) utilized 400 μm culets with a 380 μm sample chamber and ruby R1 fluorescence calibration, whereas run 2 (1.4–49.7 GPa) employed 200 μm culets with a 180 μm hole and relied on the diamond Raman edge shift for pressure determination. In both cases, four platinum leads were arranged in a standard four-probe geometry.

In situ high-pressure synchrotron XRD experiments were performed at the 4W2 beamline station of the Beijing Synchrotron Radiation Facility (BSRF) with a wavelength of 0.6199 Å. A DAC equipped with 200 μm culets and a pre-indented gasket with a 65 μm sample hole was used for pressure generation. A 4:1 methanol–ethanol mixture was used as the pressure- transmitting medium, ensuring quasi-hydrostatic conditions upon compression. The diffraction patterns were analyzed via Rietveld refinement using the GSAS software package.

First-principles calculations were performed using the Vienna *ab initio* simulation package (VASP) within the framework of density functional theory (DFT). The generalized gradient approximation (GGA) with the Perdew–Burke–Ernzerhof (PBE) functional was employed to describe the exchange–correlation energy. The plane-wave cutoff energy was set to 600 eV, and a convergence criterion of 10^{-8} eV was adopted for the self-consistent field calculations. The DFT-D3 method was utilized to model the vdW interactions between layers, and the DFT + U method with a Hubbard U value of 3.0 eV was applied to account for the correlation effects of Nb 4d electrons. Post-processing of the electronic properties was conducted using the VASPKIT program.

3. Results and discussion

Figure 1(a) depicts the crystal structure of 2H-$NbSe_2$, which crystallizes in the hexagonal space group $P6_3/mmc$. Within each Se–Nb–Se layer, the Nb atoms adopt a trigonal prismatic coordination geometry, bonded to six surrounding Se atoms. The ambient-pressure XRD pattern shown in Fig. 1(b) matches well with the standard JCPDS card for 2H-$NbSe_2$, exhibiting sharp Bragg reflection peaks that indicate high phase purity. The SEM and HRTEM images in Figs. 1(c) and 1(d) reveal the typical layered morphology of 2H-$NbSe_2$. As shown in Fig. 1(d), the observed lattice spacing is approximately 0.29 nm, corresponding to the (101) plane of the hexagonal phase. These features confirm the high crystallinity of the samples.

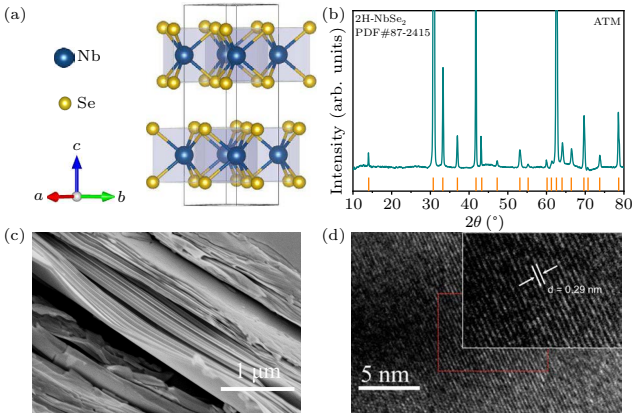


Fig. 1. (a) Schematic diagram of 2H-$NbSe_2$. The larger blue spheres and smaller yellow spheres represent Nb and Se atoms, respectively. (b) XRD pattern of $NbSe_2$ under ambient pressure, corresponding to the $P6_3/mmc$ space group. (c) SEM and (d) HRTEM images of 2H-$NbSe_2$.

To evaluate the evolution of the superconducting properties of 2H-$NbSe_2$ under compression, high-pressure electrical transport measurements were performed. As shown in Figs. 2(a) and 2(b), two independent runs of four-probe resistance measurements were conducted up to pressures of 13.1 GPa and 49.7 GPa, respectively. Prior to the emergence of the superconducting state, the resistance decreases monotonically with decreasing temperature over the entire pressure

range, confirming the metallic nature of 2H-$NbSe_2$ (Fig. S1). The suppression of the charge density wave (CDW) transition and the slightly lower T_c compared to previous literature at the initial pressure are attributed to pronounced disorder.[27,28] The T_c–P phase diagram is summarized in Fig. 2(c). The results from the two experimental runs are highly consistent; thus, the dome-shaped evolution of T_c confirms the reliability of the different pressure calibration methods. T_c reaches a maximum of approximately 6.2 K at around 10 GPa. Beyond this critical pressure, T_c decreases at a rate of 0.008 K/GPa. This dome-shaped superconducting phase diagram is consistent with observations in other layered TMDs.[29–31] Furthermore, as shown in Fig. 2(d), the room-temperature resistance exhibits a non-monotonic pressure dependence. It reaches a minimum near 10 GPa and then increases anomalously upon further compression. The dome-shaped P–T_c diagram is often attributed to the competition between CDW and superconductivity;[32–35] however, the electrical resistance measurements indicate that the suppression of the CDW is caused by pronounced disorder in 2H-$NbSe_2$. Therefore, the influence of CDW on the T_c variation can be excluded. This behavior likely correlates with anomalies in carrier concentration and mobility, as well as enhanced electron–phonon scattering in the high-pressure regime.[29,36,37] To probe the scattering mechanisms underlying this evolution, low-temperature resistivity data were analyzed using the power-law formula

$$R = R_0 + AT^n, \tag{1}$$

where R_0, A, and n denote the residual resistance, the scattering prefactor, and the inelastic scattering exponent, respectively. As shown in Fig. 3(e), the residual resistance R_0 decreases with increasing pressure up to 11 GPa, indicative of reduced impurity scattering likely due to lattice densification. However, above this critical pressure, R_0 exhibits an anomalous increase. This behavior is attributed to the formation of covalent-like interlayer bonds, which introduce structural disorder and concurrently suppress T_c. While pressure-induced sample thinning modifies the geometric factor, this effect varies monotonically with compression. Consequently, the observed non-monotonic evolution of the resistance originates from changes in its intrinsic properties. Similar trends

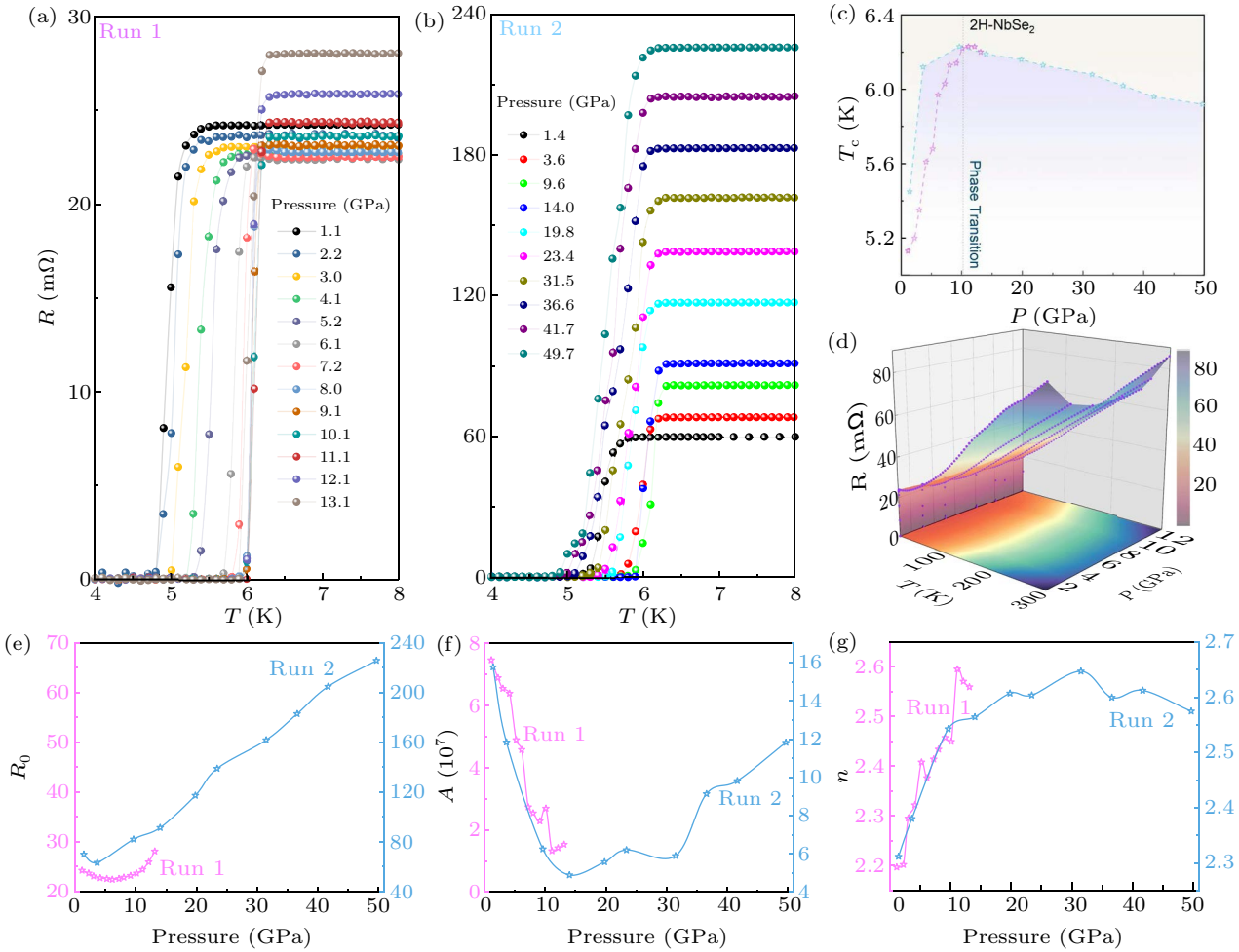


Fig. 2. Temperature-dependent resistance curves measured at pressures ranging from (a) 1.1 GPa to 13.1 GPa and (b) 1.4 GPa to 49.7 GPa. (c) T_c–P phase diagram of 2H-$NbSe_2$, where pink and blue stars denote the T_c values obtained from run 1 and run 2, respectively. (d) Three-dimensional contour plot of resistance as a function of temperature and pressure. Pressure evolution of the power-law fitting parameters: (e) R_0, (f) A, and (g) n.

have been observed in the isostructural compounds 2H-TaS_2 and 1T-$TaSe_2$.[38–40] Figures 3(f) and 3(g) display the pressure dependence of the scattering prefactor A and the exponent n, which characterize the inelastic electron scattering processes in 2H-$NbSe_2$. Both parameters undergo discontinuous changes at the critical pressure, with n increasing from approximately 2.2 to 2.6. Throughout the investigated pressure range, the value of n deviates from both the standard Fermi-liquid value ($n = 2$) and the conventional electron–phonon scattering limit ($n = 5$), signaling non-Fermi-liquid behavior. These observations suggest that the dominant scattering mechanism is neither simple electron–electron nor electron–phonon scattering but is instead consistent with phonon-assisted s–d interband scattering.[39,41,42]

To investigate the pressure-induced lattice rearrangements of 2H-$NbSe_2$, XRD patterns were analyzed over the pressure range of 1.6–55.4 GPa. As depicted in Fig. 3(a), at 1.6 GPa, the diffraction peaks can be indexed to the 2H structure with space group $P6_3/mmc$, exhibiting pronounced preferred orientation. With increasing pressure, all diffraction peaks shift toward higher angles due to lattice compression. Notably, the absence of new peaks up to 55.4 GPa underscores the structural stability of 2H-$NbSe_2$ under high pressure.

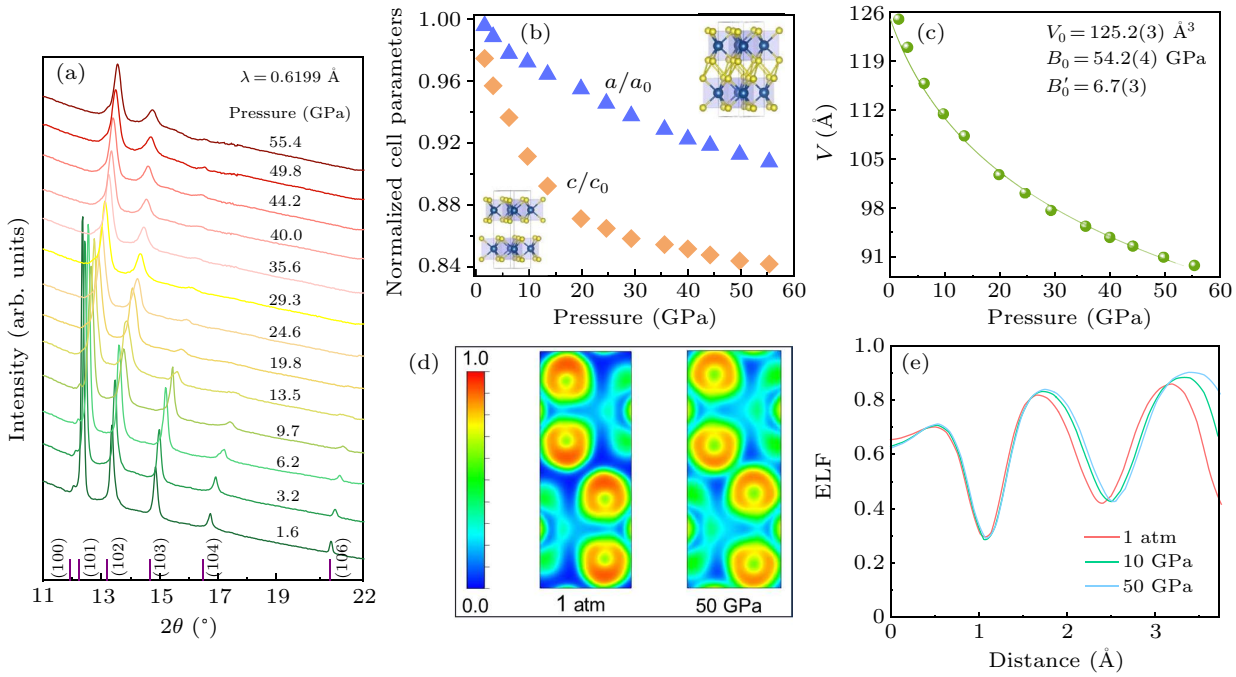


Fig. 3. (a) XRD patterns of 2H-$NbSe_2$ collected at pressures ranging from 1.6–55.4 GPa. (b) Pressure evolution of lattice parameters a and c. The inset shows schematic diagrams of the structure of $NbSe_2$ at 0 GPa and 50 GPa. (c) Pressure-dependent unit-cell volume. The solid green line represents a fit to the experimental data using the third-order B–M EOS. (d) ELF contour maps of the interlayer Se–Se region at 0 GPa and 50 GPa. (e) ELF line profiles along the interlayer Se–Se bond path at 0 GPa, 10 GPa, and 50 GPa.

To further elucidate the pressure-induced structural evolution, Figs. 3(b) and 3(c) display the variation of lattice parameters and unit-cell volume. Fitting the P–V data to a third-order Birch–Murnaghan (B–M) equation of state (EOS) yields an ambient-pressure bulk modulus of $B = 54.2(4)$ GPa, which is in good agreement with previous literature.[43,44] Upon compression, both a and c decrease; however, the c axis contracts more rapidly than the a axis. This anisotropy reflects the weak vdW interactions between adjacent layers compared to the robust in-plane covalent bonding. With increasing pressure, the interlayer Se–Se distance decreases drastically, substantially enhancing the interlayer coupling. Consequently, the interlayer forces become comparable to the intralayer covalent bonding strength. Notably, the axial compression ratio $(\Delta c/c)/(\Delta a/a)$ and the c/a ratio exhibit discontinuous changes upon compression, as shown in Fig. S2. Around 10 GPa, the pressure dependence of lattice parameters a and c changes abruptly. Upon further compression, similar to the behavior of the c/a ratio, the variation of the lattice parameters gradually becomes nearly constant, suggesting that the structural transition is largely complete. Since no significant discontinuity in the unit-cell volume is detected in Fig. 3(c), this anomaly is identified as a second-order isostructural transition, marking the transformation from a quasi-2D to a 3D structural state. Furthermore, the corresponding Rietveld refinements of XRD patterns at 9.7 and 13.5 GPa are presented in Fig. S3; the *in situ* XRD patterns were extracted from Fig. 3(a). With increasing pressure, all diffraction peaks shift toward higher angles without the emergence of any new peaks, and these XRD patterns can be well fitted, indicating that 2H-$NbSe_2$ retains the $P6_3/mmc$ space group above 10 GPa. Combined with theoretical calculations, as shown in Fig. S4, 2H-$NbSe_2$ under-

goes a second-order isostructural transition at ∼ 10 GPa. Subsequently, interlayer quasi-covalent bonds form near 20 GPa, suggesting the completion of the structural transition from quasi-2D to 3D. As the pressure increases up to 50 GPa, the interlayer Se–Se distance gradually decreases, while the interlayer covalent bonding is maintained. This dimensional transition is believed to underpin the anomalous dome-shaped superconducting behavior observed under pressure.

To elucidate the effect of pressure on interlayer bonding in 2H-$NbSe_2$, the electron localization function (ELF) of the Se–Se atoms between adjacent layers was computed from 0 to 50 GPa, as demonstrated in Fig. 3(d). As pressure increases, the steady contraction of the Se–Se interlayer distance is accompanied by a marked rise in the ELF within the interstitial region. This charge accumulation signals the emergence of quasi-covalent bonding between the layers.[45–48] This evolution is further quantified by the ELF line cuts along the Se–Se bond path, shown in Fig. 3(e). At ambient pressure, the ELF minimum between Se atoms is negligible, characteristic of weak vdW interactions. By 50 GPa, however, this value exceeds 0.4, a threshold consistent with substantial covalent character. This electronic transition provides a microscopic basis for the structural transition observed in the XRD analysis.

The electronic properties of 2H-$NbSe_2$ under pressure were further investigated via DFT calculations. Figure 4 displays the band structure and corresponding Fermi-surface evolution. As illustrated in Figs. 4(a) and 4(d), under ambient pressure, the band structure of 2H-$NbSe_2$ exhibits multiband characteristics. The Fermi surface consists of Nb 4d-derived sheets centered at the Γ and K points, and a small Se 4p-derived pocket centered at the Γ point, consistent with previous literature.[49] Upon compression to 10 GPa, as shown in Figs. 4(b) and 4(e), this central Se 4p pocket vanishes, indicative of a Lifshitz transition. The reduced density of states (DOS) at the Fermi level (E_F) is also confirmed by the calculated total DOS (TDOS) and partial DOS (PDOS) of 2H-$NbSe_2$ at 0 GPa, 10 GPa, and 50 GPa, as shown in Fig. S5. Initially, as pressure increases from 0 GPa to 10 GPa, charge is transferred from the shrinking Se 4p pocket to the Nb 4d-derived cylinders, which is consistent with previous literature.[26] This electronic instability necessitates structural re-optimization and modifies the electron–phonon interaction strength, thereby driving the formation of interlayer quasi-covalent bonds and the observed isostructural transition. The charge transfer enhances superconducting pairing, thereby increasing T_c. Upon further compression, the DOS at E_F decreases above 10 GPa, as also demonstrated in Figs. 4(c) and 4(f). The bands crossing E_F exhibit pronounced bandwidth broadening, and T_c subsequently decreases with increasing pressure. The Fermi-surface reconstruction and associated DOS evolution at E_F are key to understanding the non-monotonic superconducting behavior in layered dichalcogenides.

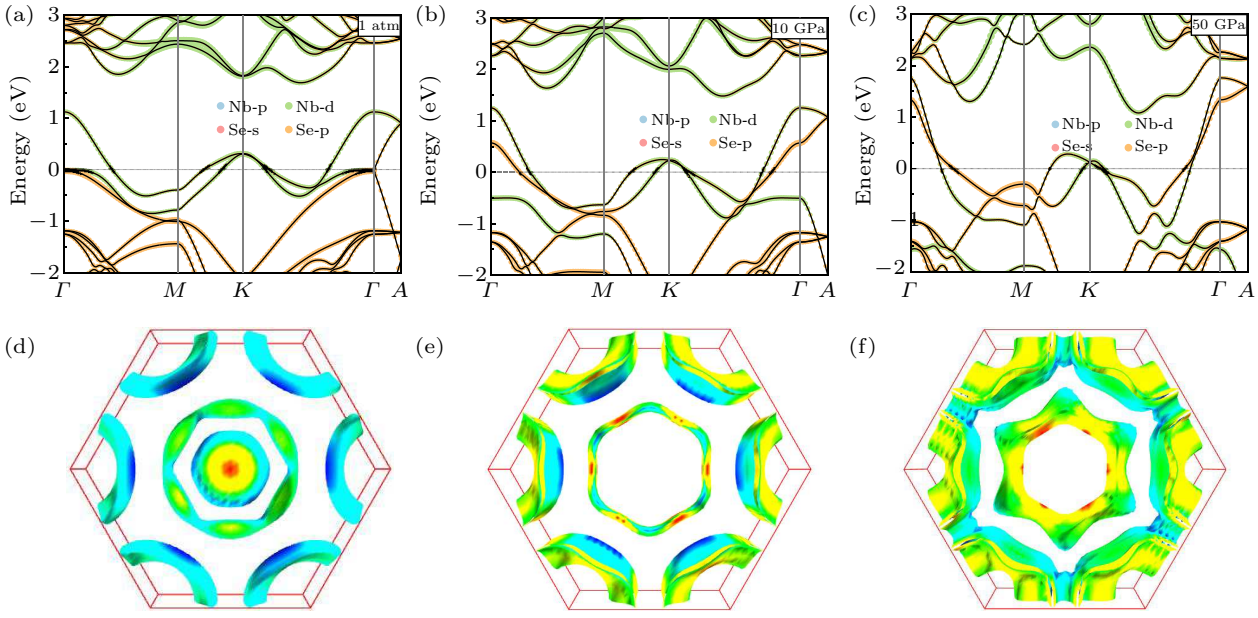


Fig. 4. Calculated DFT band structures of 2H-$NbSe_2$ at (a) 0 GPa, (b) 10 GPa, and (c) 50 GPa. The size of the dots is proportional to the spectral weight. Evolution of the three-dimensional Fermi surface of 2H-$NbSe_2$ at (d) 0 GPa, (e) 10 GPa, and (f) 50 GPa, respectively.

4. Conclusion

In summary, the superconducting properties and structural evolution of 2H-$NbSe_2$ under pressure have been systematically investigated through electrical transport measurements and high-pressure XRD. Upon compression, 2H-$NbSe_2$ exhibits a second-order isostructural transition, marking a crossover from a quasi-2D to a 3D state. The resulting dome-shaped T_c–P phase diagram arises from competing mecha-

nisms, where enhanced interlayer coupling initially promotes superconductivity, while the eventual suppression of T_c is driven by enhanced impurity scattering and a reduced density of states at the Fermi level (E_F). By identifying interlayer coupling and Fermi-surface reconstruction as the key drivers of this non-monotonic superconducting behavior, this work offers a valuable framework for engineering high-T_c phases in layered 2D materials.

Acknowledgment

This work was supported by the Doctoral Research Startup Fund of Liaoning Province (Grant No. 2025-BS-0867).

References

[1] Nandi M, Dutta S, Thamizhavel A and Dhar S K 2024 *Phys. Rev. B* **110** 165107
[2] Ichinokura S, Tokuda K, Toyoda M, Tanaka K, Saito S and Hirahara T 2024 *ACS Nano* **18** 13738
[3] Xiao G J, Geng T and Zou B 2020 *ACS Mater. Lett.* **2** 1233
[4] Mao H K, Chen X J, Ding Y, Li B and Wang L 2018 *Rev. Mod. Phys.* **90** 015007
[5] Chen K Y, Wang N N, Yin Q W, Gu Y H, Jiang K, Tu Z J, Gong C S, Uwatoko Y, Sun J P, Lei H C, Hu J P and Cheng J G 2021 *Phys. Rev. Lett.* **126** 247001
[6] Ma L, Wang K, Xie Y, Yang X, Wang Y Y, Zhou M, Liu H Y, Yu X H, Zhao Y S, Wang H B, Liu G T and Ma Y M 2022 *Phys. Rev. Lett.* **128** 167001
[7] Chen W H, Semenok D V, Kvashnin A G, Huang X L, Kruglov I A, Galasso M, Song H, Duan D F, Goncharov A F, Prakapenka V B, Oganov A R and Cui T 2021 *Nat. Commun.* **12** 273
[8] Chang C, Chen W, Chen Y, *et al.* 2021 *Acta Phys. Sin.* **37** 2108017
[9] Rohaizad N, Mayorga Martinez C C, Fojtu M, Latiff N M and Pumera M 2021 *Chem. Soc. Rev.* **50** 619
[10] Sebastian A, Pendurthi R, Choudhury T H, Redwing J M and Das S 2021 *Nat. Commun.* **12** 693
[11] Jia L G, Zhang C, Gao F, Chen Y Y, Zhou L L, Zhou F D, Han X, Zhang T, Sánchez-Portal D and Gao S 2025 *Chin. Phys. Lett.* **42** 080712
[12] Rajaji V, Dutta U, Sreeparvathy P C, Sarma S C, Sorb Y A, Joseph B, Sahoo S, Peter S C, Kanchana V and Narayana C 2018 *Phys. Rev. B* **97** 085107
[13] Zhou Y H, Chen C H, Zhou Y, Chen X L, Gu C C, An C, Zhang B W, Yuan Y F, Wu H, Zhang R R, Zhang L L, Zhu X D, Yang X P and Yang Z R 2019 *Phys. Rev. B* **99** 125104
[14] Saqib H, Rahman S, Zhao Y S, Cazorla C, Errandonea D, Susilo R, Zhuang Y K, Huang Y W, Chen B and Dai N 2021 *J. Phys. Chem. Lett.* **12** 9859
[15] Dutta U, Malavi P S, Sahoo S, Joseph B and Karmakar S 2018 *Phys. Rev. B* **97** 060503
[16] Dong Q, Li Q J, Li S J, Shi X H, Niu S F, Liu S J, Liu R, Liu B, Luo X, Si J G, Lu W J, Hao N, Sun Y P and Liu B B 2021 *npj Quantum Mater.* **6** 20
[17] Dong Q, Pan J, Li S J, Fang Y Q, Lin T, Liu S, Liu B, Li Q J, Huang F Q and Liu B B 2022 *Adv. Mater.* **34** 2103168
[18] Yokoya T, Kiss T, Chainani A, Shin S, Nohara M and Takagi H 2001 *Science* **294** 2518
[19] Huang C L, Lin J Y, Chang Y T, Sun C P, Shen H Y, Chou C C, Berger H, Lee T K and Yang H D 2007 *Phys. Rev. B* **76** 212504
[20] Foner S and McNiff Jr E 1973 *Phys. Lett. A* **45** 429
[21] Zhang F, Hou X Y, Jiang Y X, Zhang Z Y, Tu Y B, Zhu X D, Chen G F and Shan L 2024 *Chin. Phys. B* **33** 067401
[22] Zhang J N, Wang G, Han T Y and Huang H 2025 *Chin. Phys. B* **34** 057401
[23] Jerome D, Grant A and Yoffe A 1971 *Solid State Commun.* **9** 2183
[24] Jones Jr R, Shanks H, Finnemore D and Morosin B 1972 *Phys. Rev. B* **6** 835
[25] Smith T, Shelton R and Schwall R 1974 *J. Phys. F: Met. Phys.* **4** 2009
[26] Suderow H, Tissen V, Brison J, Martínez J and Vieira S 2005 *Phys. Rev. Lett.* **95** 117006
[27] Xu S X, Gao J J, Liu Z Y, Chen K Y, Yang P T, Tian S J, Gong C S, Sun J P, Xue M A Q, Gouchi J, Luo X, Sun Y P, Uwatoko Y, Lei H C, Wang B S and Cheng J G 2021 *Phys. Rev. B* **103** 224509
[28] Cho K, Konczykowski M, Teknowijoyo S, Tanatar M A, Guss J, Gartin P B, Wilde J M, Kreyssig A, McQueeney R J, Goldman A I, Mishra V, Hirschfeld P J and Prozorov R 2018 *Nat. Commun.* **9** 2796
[29] Lv X D, Song H, Chen K, Liu S R, Huang Y P, Fang Y Q, Shen Z X and Cui T 2014 *Sci. China-Phys. Mech. Astron.* **67** 128211
[30] Guo J, Huang C, Luo H X, Yang H X, Wei L L, Cai S, Zhou Y Z, Zhao H C, Li X D, Li Y C, Yang K, Li A G, Sun P J, Li J Q, Wu Q, Cava R J and Sun L L 2022 *Phys. Rev. Mater.* **6** L051801
[31] Joe Y I, Chen X M, Ghaemi P, Finkelstein K D, de la Pena G A, Gan Y, Lee J C T, Yuan S, Geck J, MacDougall G J, Chiang T C, Cooper S L, Fradkin E and Abbamonte P 2014 *Nat. Phys.* **10** 421
[32] Nie J Y, Yang X F, Chen K Y, Liu X Q, Xia W, Wang J, Zhang R, Dai D Z, Zhao C C and Tu C P 2025 *Chin. Phys. Lett.* **42** 070713
[33] Yan L M, Bu K J, Li Z Y, Zhang Z H, Xia W, Li M T, Li N N, Guan J Y, Liu X Q, Ning J H, Zhang D Z, Guo Y F, Wang X and Yang W G 2024 *Nano Lett.* **24** 6002
[34] Yan D, Zeng L Y, Zeng Y J, Lin Y S, Yin J J, Wang M, Wang Y H, Yao D X and Luo H X 2022 *Chin. Phys. B* **31** 037406
[35] Majumdar A, VanGennep D, Brisbois J, Chareev D, Sadakov A V, Usoltsev A S, Mito M, Silhanek A V, Sarkar T, Hassan A, Karis O, Ahuja R and Abdel-Hafiez M 2020 *Phys. Rev. Mater.* **4** 084005
[36] Ke F, Yang J, Liu C L, Wang Q L, Li Y Q, Zhang J K, Wu L, Zhang X, Han Y H, Wu B J, Ma Y Z and Gao C X 2013 *J. Phys. Chem. C* **117** 6033
[37] Li Y F, Zhou Y H, Guo Z P, Han F, Chen X L, Lu P C, Wang X F, An C, Zhou Y, Xing J, Du G, Zhu X Y, Yang H, Sun J, Yang Z R, Yang W G, Mao H K, Zhang Y H and Wen H H 2017 *npj Quantum Mater.* **2** 66
[38] Lin T, Wang X J, Chen X, Liu X B, Luo X, Li X, Jing X L, Dong Q, Liu B, Liu H Y, Li Q J, Zhu X B and Liu B B 2021 *Inorg. Chem.* **60** 11385
[39] Zhao X M, Zhang K, Cao Z Y, Zhao Z W, Struzhkin V V, Goncharov A F, Wang H K, Gavriliuk A G, Mao H K and Chen X J 2020 *Phys. Rev. B* **101** 134506
[40] Mazin I I, Andersen O K, Jepsen O, Dolgov O V, Kortus J, Golubov A A, Kuz'menko A B and van der Marel D 2002 *Phys. Rev. Lett.* **89** 107002
[41] Forsythe D, Julian S R, Bergemann C, Pugh E, Steiner M J, Alireza P L, McMullan G J, Nakamura F, Haselwimmer R K W, Walker I R, Saxena S S, Lonzarich G G, Mackenzie A P, Mao Z Q and Maeno Y 2002 *Phys. Rev. Lett.* **89** 166402
[42] Li S J, Dong Q, Feng J J, Wang Y J, Hou M Q, Deng W, Susilo R A, Li N N, Dong H L, Wan S, Gao C X and Chen B 2021 *Inorg. Chem.* **60** 7857
[43] Mkrtchyan V, Kumar R, White M, Yanxon H and Cornelius A 2018 *Chem. Phys. Lett.* **692** 249
[44] Chen G P, Bykova E, Bykov M, Edmund E, Cao Z Y, Chen X J, Smith J S, Chariton S, Prakapenka V B and Goncharov A F 2022 *Phys. Rev. B* **105** 224114
[45] Xu M, Jakobs S, Mazzarello R, Cho J Y, Yang Z, Hollermann H, Shang D S, Miao X S, Yu Z H, Wang L and Wuttig M 2017 *J. Phys. Chem. C* **121** 25447
[46] Liu J, Zhu J M, Yu H Y, Zhang Z H, Wu G, Yao A D, Pan L Y, Bao K and Cui T 2024 *Inorg. Chem.* **63** 12248
[47] Yan X Z, Chen Y M, Xiang S K, Kuang X Y, Bi Y and Chen H Y 2016 *Phys. Rev. B* **93** 214112
[48] Jin Y Y, Zhang J Q, Ling S, Wang Y Q, Li S, Kuang F G, Wu Z Y and Zhang C Z 2022 *Chin. Phys. B* **31** 116104
[49] Rossnagel K, Seifarth O, Kipp L, Skibowski M, Voss D, Krüger P, Mazur A and Pollmann J 2001 *Phys. Rev. B* **64** 235119